

# Space-dependent turbulence model aggregation using machine learning

M. de Zordo-Banliat<sup>(1,2)</sup>, G. Dergham<sup>(1)</sup>, X. Merle<sup>(2)</sup>, P. Cinnella<sup>(3)</sup>

<sup>(1)</sup> Safran Tech, Digital Sciences & Technologies Department, Rue des Jeunes Bois, Châteaufort, 78114 Magny-Les-Hameaux, France

<sup>(2)</sup> DynFluid Laboratory - Arts et Métiers ParisTech - 151 boulevard de l'Hôpital, 75013 Paris, France

<sup>(3)</sup> Institut Jean Le Rond D'Alembert - Sorbonne Université - 4 Place Jussieu, 75005 Paris, France  
gregory.dergham@safrangroup.com

---

## Abstract

Computational models of fluid flows based on the Reynolds-averaged Navier–Stokes (RANS) equations supplemented with a turbulence model are the golden standard in engineering applications. A plethora of turbulence models and related variants exist, none of which is fully reliable outside the range of flow configurations for which they have been calibrated. Thus, the choice of a suitable turbulence closure largely relies on subjective expert judgement and engineering know-how. In this article, we propose a data-driven methodology for combining the solutions of a set of competing turbulence models. The individual model predictions are linearly combined for providing an ensemble solution accompanied by estimates of predictive uncertainty due to the turbulence model choice. First, for a set of training flow configurations we assign to component models high weights in the regions where they best perform, and vice versa, by introducing a measure of distance between high-fidelity data and individual model predictions. The model weights are then mapped into a space of features, representative of local flow physics, and regressed by a Random Forests (RF) algorithm. The RF regressor is finally employed to infer spatial distributions of the model weights for unseen configurations. Predictions of new cases are constructed as a convex linear combination of the underlying models solutions, while the between model variance provides information about regions of high model uncertainty. The method is demonstrated for a class of flows through the compressor cascade NACA65 V103 at  $Re \simeq 3 \times 10^5$ . The results show that the aggregated solution outperforms the accuracy of individual models for the quantity used to inform the RF regressor, and performs well for other quantities well-correlated to the preceding one. The estimated uncertainty intervals are generally consistent with the target high-fidelity data. The present approach then represents a viable methodology for a more objective selection and combination of alternative turbulence models in configurations of interest for engineering practice.

*Keywords:* turbulent flows, RANS equations, RANS models, model mixture, space-dependant weights, NACA65

---

## 1. Introduction

Scientific modeling is the process of describing the physical reality via mathematical equations, based on a set of simplifying assumptions and on experimental observation of a system. The modeling hypotheses determine the

mathematical structure of the model, called a model class, and limit the validity of its predictions. A specific model is then singled-out from the class by specifying a set of closure parameters, generally adjusted to fit experimental observation. Such a process is called *calibration*. Due to the underlying modeling assumptions and to observation errors corrupting experimental data, hence closure parameters, predictions based on a model are affected by uncertainties on both the model form (called epistemic uncertainty) and on the closure parameters (parametric uncertainty) [1].

In the present work we focus on Computational Fluid Dynamics (CFD) models, i.e. computer models for solving the governing equations for fluid flows:

$$\mathcal{NS}[\mathbf{q}(\mathbf{x}, t); S] = 0 \quad (1)$$

where  $\mathcal{NS}$  is the Navier-Stokes partial differential operator,  $\mathbf{q}(\mathbf{x}, t)$  is the state variable vector (e.g. pressure, velocity,...),  $\mathbf{x}$  is a vector of coordinates in the geometrical space,  $t$  is the time and  $S$  is a set of parameters determining the flow conditions, such as the geometry and the initial and boundary conditions, which we call a flow *scenario*. Very broad model classes, better called modeling "levels", can be identified according to the inclusion or not of some physical effects. We distinguish for instance inviscid from viscous models. For viscous flows characterized by high values of the Reynolds number ( $Re = UL/\nu$ , with  $U$  a characteristic velocity scale,  $L$  a length scale, and  $\nu$  a reference value for the fluid kinematic viscosity) several modeling levels can be identified, according to the strategy used to account for turbulent motions. Direct Numerical Simulations (DNS) solve for all turbulent motions by seeking the solution of the discretised form of (1):

$$\mathcal{D}[\mathcal{NS}[\mathbf{q}(\mathbf{x}, t); S]] = 0, \quad (2)$$

with  $\mathcal{D}$  a discretisation operator on a fine-grained space and time mesh. The computational cost of DNS models scales as  $Re^{11/4}$  for DNS [2], making them prohibitively expensive for the high-Reynolds number flows of interest. On the other hand, by applying a coarse-grained operator to Eq. (1), state variables can be split into a coarse-grained part  $\widetilde{\mathbf{q}}$  and an unresolved  $\mathbf{q}'$  part:  $\mathbf{q} = \widetilde{\mathbf{q}} + \mathbf{q}'$ . Large-Eddy Simulations (LES), consisting in filtering the small scales and resolving the large, energetic ones, require a number of grid points of order of  $Re^{13/7}$  for resolving wall-bounded flows [3], which strongly limits their routine use for practical engineering problems. As a result, engineering design mostly relies on lower-fidelity models such as the Reynolds-averaged Navier–Stokes (RANS) equations. The latter use a similar decomposition to LES whereby the filter is replaced by a statistical averaging operator:

$$\widetilde{\mathcal{NS}}[\mathbf{q}(\mathbf{x}, t); S] = 0 \quad \Rightarrow \quad \mathcal{NS}[\widetilde{\mathbf{q}}; S] + \nabla \cdot \mathcal{F}(\widetilde{\mathbf{q}}, \mathbf{q}') = 0 \quad (3)$$

Thus the RANS equations solve only for mean flow motions.  $\mathcal{F}(\widetilde{\mathbf{q}}, \mathbf{q}')$  represents the contribution of turbulent flow scales to the transport of momentum and energy and is accounted for by supplementing the RANS equations with additional constitutive relations. The latter, called a turbulence model, express the so-called Reynolds stress tensor (a

measure of turbulent transport of momentum) as a function of mean field variables:

$$\mathcal{NS}[\tilde{\mathbf{q}}_m; S] + \nabla \cdot \mathcal{F}_m(\tilde{\mathbf{q}}_m; \boldsymbol{\theta}_{\mathcal{F}_m}) = 0 \quad (4)$$

where  $\tilde{\mathbf{q}}_m$  is an approximation of  $\tilde{\mathbf{q}}$  under the chosen turbulence model, and  $\boldsymbol{\theta}_{\mathcal{F}_m}$  is a vector of parameters associated with the turbulence model  $\mathcal{F}_m$ . The RANS equations (4) are then numerically solved by applying some discretisation operator  $\mathcal{D}$ :

$$\mathcal{D}[\mathcal{NS}[\tilde{\mathbf{q}}_m; S] + \nabla \cdot \mathcal{F}_m(\tilde{\mathbf{q}}_m; \boldsymbol{\theta}_{\mathcal{F}_m})] = 0 \quad (5)$$

Only steady solutions are sought in this work, and we denote  $\tilde{\mathbf{q}}_m^\dagger = \tilde{\mathbf{q}}_m^\dagger(\mathbf{x})$  the numerical solution of the discrete equations (5). For a Quantity of Interest (QoI)  $\delta$ , post-processed from the computed state vector  $\tilde{\mathbf{q}}_m^\dagger$ , the whole process may be written in short as

$$\delta = M(\mathbf{x}; S, \mathcal{F}_m, \boldsymbol{\theta}_{\mathcal{F}_m}) \quad (6)$$

where  $M$  is the post-processed CFD model output, which depends on the geometrical space, the operating conditions  $S$ , and the turbulence model. For brevity,  $S$ ,  $\mathcal{F}_m$  and  $\boldsymbol{\theta}_{\mathcal{F}_m}$  are omitted when irrelevant.

Despite the plethora of turbulence models proposed in the literature for more than a century, determining a turbulent closure universally valid for any kind of flow remains a formidable challenge (see [4, 5] for overviews). Existing turbulence models can be classified according to their levels of complexity, and a number of variants and corrections exist for different flow features such as pressure gradients, separation, vortices, rotations, shock waves, etc. The reader is referred to the NASA repository <https://turbmodels.larc.nasa.gov>, for the description of some widely-used turbulence models. Assessment against academic and industrial applications shows that the choice of the turbulence model and of the associated closure parameters  $\boldsymbol{\theta}_{\mathcal{F}_m}$  may cause large variability in CFD predictions, which in turn may be critical for decision making [6].

Early attempts to quantify uncertainties in RANS models are due to Cheung et al. [7], Oliver and Moser [8], Emory et al. [9] and Edeling et al. [10]. Such studies treat turbulence modeling uncertainties in a probabilistic framework: instead of producing a single deterministic prediction associated with a model form and a set of parameters, they try to estimate the probability distribution of model outputs, conditioned on some random inputs. The analysis is conducted either by perturbing directly the Reynolds stress anisotropy tensor computed with a baseline LEVM [9, 11, 12] or by treating the turbulence model closure parameters as random variables with associated probability distributions [13, 7, 14, 15]. While the first approach accounts for model-form uncertainties, the second does not. In turn, the first approach is intrusive in the sense that its implementation involves modifications of the RANS solver, while in the second one the stochastic parameters can be just fed as inputs to the CFD solver and propagated by using a suitable (non intrusive) uncertainty quantification method.

An attractive and non-intrusive approach for quantifying model-form uncertainty is represented by multi-model, or ensemble, statistical methods. For instance, [16] used the Demster-Shafer evidence theory along with the  $k-\epsilon$  and  $k-\omega$  turbulence models to quantify the variability of CFD simulations. More recently, [10] explored a Bayesian framework,

namely, Bayesian Model-Scenario Averaging (BMSA), to calibrate and combine the predictions obtained from a set of competing baseline LEVM models calibrated on various data sets (scenarios). BMSA has been successfully applied to provide stochastic predictions for a variety of flows, including 3D wings [17] and compressor cascades [18, 19].

BMSA, and Bayesian Model Averaging (BMA) [20, 21] from which it originates, may be interpreted as stochastic variants of the Model Aggregation framework (Stoltz [22], Deswarte *et al.* [23], Devaine *et al.* [24]), also referred-to as Sequential Model Aggregation (SMA). The latter belongs to a wider class of methods, denominated Multiplicative Weight Updating Algorithms [25], first introduced in the late 80's [26] and further developed in [27, 28, 29]. Such methods aim at combining multiple predictions stemming from various models –also termed experts or forecasters– to provide a global, enhanced, solution — the ‘wisdom of crowd’ paradigm, well-known in Machine Learning. In SMA, weights are computed by using the Exponentially Weighted Average (EWA) [23], which may be interpreted as a loss function. In such an approach the parameters intrinsic to the individual models may be updated or not during the training process. In BMA, the predictions of the competing models are weighted by posterior model probabilities, computed through the Bayes’ theorem of inverse probability. Model Aggregation is generally not applied to space-dependent predictions while BMA has been. In such case, however, the same BMA weights are assigned throughout the spatial domain. Spatially-constant weighting of different RANS-model solutions is not optimal, since prior knowledge about RANS indicates that the accuracy of models may vary according to the local flow physics. In principle, one would like to assign higher weights to the best-performing models in each region.

Other classes of ensemble methods allow space-varying weights [30, 31, 32]. In Mixture-of-local-Experts [33], also referred-to as Mixture-of-Experts [34] or Mixture Models, the input feature space (covariate space) is softly split into partitions where the locally best-performing models are assigned higher weights. The soft partitioning is accomplished through parametric gate functions, or a network of hierarchical gate functions [35], that rank the model outputs with probabilities. For promoting the best models in each partition, the softmax function [36, 37] — a smoothed version of the winner-takes-all model — is employed to build the probabilities. Parameters associated with the component models and with the gate functions are trained simultaneously through the Expectation Maximisation algorithm [38], or improved versions [39]. Although the Mixture-of-Experts method originates from a stochastic formulation, the model output is ultimately a deterministic convex linear combination of individual expert outputs. Additionally, Mixture-of-Experts tends to promote a single best model in every soft partition, thus accounting for the spatial variation of the best model but strongly neglecting the uncertainty in model choice.

In the attempt of combining the best features of BMA and Mixture-of-Experts, Yu *et al.* [40] proposed an improved version of the BMA, called “Clustered Bayesian Averaging” (CBA), allowing for space-varying weighting of the component models in different regions of the covariate space. For that purpose, they computed so-called “local Bayes factors”, which were input to a clustering algorithm determining a spatial partition. Specifically, the Classification And Regression Trees (CART) algorithm was employed to identify the clusters and to regress the local model Bayes factors as functions of space. At the same time, part of the data are used for iteratively updating the parameters of each component model. Predictions of a new configuration through the CBA model are finally constructed by

estimating the posterior model probabilities from the regressed local Bayes factors, and by assigning them as weights of the model mixture. The CBA algorithm has been applied successfully to hydrology [41] and solid mechanics [42], but no extensions to CFD problems have been considered up to date. CBA represents an attractive approach for estimating and improving turbulence modeling uncertainties in CFD because it provides local estimates of posterior model probabilities, used for aggregating component models into a "hypermmodel" (the model mixture) with improved predictive capabilities than the mixture components. The procedure assigns weights to the models, as function of local model performance in each flow subregion, while adjusting their parameters. The iterative update of model parameters from data improves accuracy via calibration, but it also represents a critical step of the CBA algorithm, due to the huge number of model evaluations, i.e. costly CFD solves, required in the process.

In the present paper, we propose and validate a novel space-dependent Model Aggregation (XMA) algorithm to generate mixtures of RANS solutions obtained with different turbulence models. Unlike the BMSA approach used in previous works [10, 17, 18, 19], XMA enables locally variable weights. The algorithm is inspired from both CBA and SMA, redesigned for costly CFD applications. More precisely, the original CBA algorithm is simplified to account for the high computational cost of CFD solves, and no model calibration is performed, so that local Bayes factors are no longer available. In the proposed methodology, we use instead an EWA loss function inspired from SMA to assign local model weights. The latter do not depend directly on geometrical coordinates in the physical space but on a set of well-chosen flow features, which eases generalization of the learned XMA model to different flows. The XMA algorithm is trained and applied to the prediction of flows through the compressor cascade NACA65 V103, showing better accuracy than the individual RANS models in the mixture for all flow quantities of interest.

The paper is organized as follows. In Section 2, we present the XMA methodology. Section 3 provides information about the RANS models in use and the flow configuration and reference data used in the numerical experiments. Section 4 reports a detailed assessment of the proposed method for both interpolation and extrapolation cases, and for different training datasets. Finally, the main findings are summarized in Section 5, alongside perspectives for future developments.

## 2. Space-dependent Model Aggregation (XMA)

Be  $\hat{\delta}(\mathbf{x})$  the true value of a spatially-varying flow quantity. A modeled counterpart  $\delta$  for  $\hat{\delta}$  is obtained as the output of a CFD model of the form (6), which reads:

$$\delta = M(\mathbf{x}; S, \mathcal{F}_m, \theta_{\mathcal{F}_m}).$$

We assume that all inputs  $S$  to the CFD code (geometry, boundary conditions, etc) are perfectly known and numerical errors are negligibly small, so that all deviations between the truthful quantity  $\hat{\delta}$  and the model output  $\delta$  are due to the turbulence model  $\mathcal{F}_m$  and its closure parameters  $\theta_{\mathcal{F}_m}$ .

In the aim of accounting to some extent for model-form uncertainties, while improving prediction accuracy, we do not predict  $\hat{\delta}$  using a single, uncertain model. Instead, we adopt a multi-model ensemble approach and we construct

a convex linear combination of a set of alternative RANS models, or component models, by means of weighting functions that depend on a set of flow features (introduced in Section 2.3). More precisely, we consider a discrete set of  $N_M$  models

$$\mathcal{M} = \{M_1, \dots, M_m, \dots, M_{N_M}\}$$

corresponding to  $N_M$  CFD solves of the same problem based on different turbulence models:

$$M_m = M(\mathbf{x}; S, \mathcal{F}_m, \boldsymbol{\theta}_{\mathcal{F}_m}), \quad m = 1, \dots, N_M$$

The space-dependent model aggregation (XMA) then takes the form:

$$\sum_{m=1}^{N_M} w_m M_m \quad (7)$$

where  $w_m = w_m(\mathbf{x})$  is a space-dependent weighting function associated with the  $m$ -th component model, subject to:

$$0 \leq w_m(\mathbf{x}) \leq 1, \quad \text{and} \quad \sum_{m=1}^{N_M} w_m(\mathbf{x}) = 1 \quad \forall \mathbf{x}$$

The closure parameters  $\boldsymbol{\theta}_{\mathcal{F}_m}$  associated to  $\mathcal{F}_m$  are also uncertain and could be calibrated from data (see [43, 10]). However, such a process generally requires a significant number of CFD solves for finding the best-fit values of the parameters with respect to a set of observed data. The cost can be alleviated, e.g. by using surrogate models [18], but it remains high for complex 3D configurations. For that reason, in the present study we do not attempt to update the turbulence model parameters, which are kept fixed to their nominal values for each component model. Since the closure parameters are now assigned once and for all for each turbulence model, we simplify the notation as follows:

$$M_m = M(\mathbf{x}; S, \mathcal{F}_m), \quad m = 1, \dots, N_M$$

The next step of XMA consists in inferring the weighting functions of the model mixture.

Be  $\bar{\boldsymbol{\delta}} = (\bar{\delta}_1, \dots, \bar{\delta}_d, \dots, \bar{\delta}_{N_{\hat{\delta}}})^T$  a vector of  $N_{\hat{\delta}}$  observations of the quantity  $\hat{\delta}$  at various spatial locations  $\mathbf{x}_d \in \mathbf{X}$ ,  $\mathbf{X} = \{\mathbf{x}_d\}_{d=1}^{N_{\hat{\delta}}}$ , and possibly for various flow scenarios  $S$ . To enable the use of heterogenous observations in  $\bar{\boldsymbol{\delta}}$  (i.e. corresponding to different flow properties and flow conditions), each subgroup of data is assumed to be standardized to a distribution of zero mean and unit standard deviation.

We note  $\boldsymbol{\delta}^{(m)} = (\delta_1^{(m)}, \dots, \delta_d^{(m)}, \dots, \delta_{N_{\hat{\delta}}}^{(m)})^T$  the predictions of a component model  $M_m$  at the observation locations, where  $\delta_d^{(m)} = M_m(\mathbf{x}_d)$  (we omitted the other arguments for brevity). Spatial coordinates are specific to a given flow configuration and do not possess the due invariance properties for ensuring model generalization. For that reason, we chose instead to transform the spatial fields into a well-chosen space of *features*  $\boldsymbol{\eta} = \boldsymbol{\eta}(\mathbf{x})$ , i.e. flow properties representative of the local flow physics. A similar approach is adopted, e.g., in [44] to generalize spatially-dependent

corrective fields for the turbulence model transport equations.

The mixture weighting functions are then learned in the feature space instead of the geometrical space:

$$w_m = w_m(\boldsymbol{\eta})$$

by transforming the training dataset  $\mathbf{X} = \{\mathbf{x}_d\}_{d=1}^{N_{\delta}}$  into  $\mathbf{H} = \{\boldsymbol{\eta}_d\}_{d=1}^{N_{\delta}}$ . In practice, the exact features are unknown, and features estimated from CFD depend on the turbulence model in use. Various strategies are possible, such as averaging features estimated from various models. Hereafter we chose to make each weighting function dependent on features estimated from the corresponding component model, i.e.

$$w_m = w_m(\boldsymbol{\eta}^{(m)})$$

To compute the weighting functions at points of the feature space not included in the data set, we use a supervised machine learning procedure. The weighting criteria, the machine learning regressor, and the definition of the feature space are discussed in Sections (2.1), (2.2), and (2.3), respectively.

### 2.1. Weighting criteria

Several weighting functions are available in the literature. In this work, we adapt the weighting function from the Exponentially Weighted Average (EWA) predictor, initially introduced by Deswarte *et al.* [23] for SMA, by introducing local dependence on the feature vectors:

$$w_m(\delta^{(m)}; \boldsymbol{\eta}_d^{(m)}, \bar{\delta}_d, \sigma) = \frac{g_m(\delta^{(m)}; \boldsymbol{\eta}_d^{(m)}, \bar{\delta}_d, \sigma)}{\sum_{j=1}^{N_M} g_j(\delta^{(j)}; \boldsymbol{\eta}_d^{(j)}, \bar{\delta}_d, \sigma)}, \quad m \in \{1, \dots, N_M\} \quad (8)$$

where  $g_m$  is a cost function defined by

$$g_m = \exp\left(-\frac{1}{2} \frac{(\delta^{(m)}(\boldsymbol{\eta}_d^{(m)}) - \bar{\delta}_d)^2}{\sigma^2}\right). \quad (9)$$

$g_m$  is reminiscent of a Gaussian likelihood function used in Bayesian approaches, which amplifies/damps the discrepancies between the output of the  $m$ -th model and the data. The cost function equals 1 when the model perfectly matches the data ( $\delta^{(m)}(\boldsymbol{\eta}_d^{(m)}) = \bar{\delta}_d$ ) and it tends to 0 for very large discrepancies, respectively. The squared exponential ensures a smooth variation of  $g_m$  with  $\delta^{(m)}(\boldsymbol{\eta}_d^{(m)}) - \bar{\delta}_d$ . The parameter  $\sigma$  is the learning rate of EWA, controlling how fast the departure of the model prediction  $\delta^{(m)}$  from the observed data  $\bar{\delta}$  is penalized by the cost function  $g_m$ : when  $\sigma \rightarrow \infty$ , the models are assigned uniform weights; when  $\sigma \rightarrow 0$ , the worst-performing models get weights closer to 0, while the weight of the best-performing model gets closer to 1. In other terms,  $\sigma$  controls model selection. As in [23], the optimal value of the parameter  $\sigma$  is sought by a grid search procedure. Precisely, we compute the Mean Squared

Error (MSE) between the final prediction and the observables for every point in the data set, such that :

$$\sigma_{\text{opt}} = \arg \min_{\sigma \in \Sigma} \frac{1}{N_{\tilde{\delta}}} \sum_{d=1}^{N_{\tilde{\delta}}} \left( \bar{\delta}_d - \sum_{m=1}^{N_M} w_m(\boldsymbol{\eta}_d^{(m)}; \sigma) \delta^{(m)}(\boldsymbol{\eta}_d^{(m)}) \right)^2 \quad (10)$$

where  $\Sigma$  is a grid of prescribed values for  $\sigma$ . We verified that  $\sigma$  has little influence on the model accuracy, provided the order of magnitude is correct [23].

Finally, the XMA prediction  $\delta$  of  $\hat{\delta}$  at point  $\boldsymbol{\eta}_*$  of the feature space is obtained as

$$\delta(\boldsymbol{\eta}_*) = \sum_{m=1}^{N_M} w_m(\boldsymbol{\eta}_*^{(m)}) \delta^{(m)}(\boldsymbol{\eta}_*^{(m)}) \quad (11)$$

where we omitted the dependency on  $\delta^{(m)}$ ,  $\bar{\delta}_d$  and  $\sigma$  in  $w_m$  for brevity. Note that the prediction is dependent on  $\boldsymbol{\eta}_*$ , which stands for the concatenation of feature vectors  $\boldsymbol{\eta}_*^{(m)}$  for each component model. The subscript  $*$  refers to unobserved locations in geometrical space for the training scenarios, but also to any location of a new (unseen) scenario to predict. Since the  $g_m(\boldsymbol{\eta}^{(m)})$  are known only at observation points  $\boldsymbol{\eta}_d^{(m)}$ , they are regressed across the feature space for each model  $m$  to obtain estimates of the weights at new locations  $\boldsymbol{\eta}_*$ . For that aim, a supervised regression method, presented in Section (2.2) is employed.

The predictions  $\delta^{(m)}$  given by competing models may be interpreted as the  $N_M$  possible outcomes of a discrete random variable  $\tilde{\delta}$  whose probability mass function (pmf) corresponds to the weights  $w_m$ . Thereby, Eq. (11) can be interpreted as the expected value of  $\tilde{\delta}$ :

$$\delta(\boldsymbol{\eta}_*) = E[\tilde{\delta}(\boldsymbol{\eta}_*)] = \sum_{m=1}^{N_M} w_m(\boldsymbol{\eta}_*^{(m)}) \delta^{(m)}(\boldsymbol{\eta}_*^{(m)}) \quad (12)$$

The aggregated prediction, given by (12), gives more weight to the best performing models, and less weight to the worst performing ones. As a result, it is expected to be more accurate than the individual models. Moreover, promoting the best models is done locally in space through the use of the flow features, so that each component model participates primarily at the most relevant locations.

Similarly, the predictive variance can be written as

$$\text{Var}[\tilde{\delta}(\boldsymbol{\eta}_*)] = \sum_{m=1}^{N_M} w_m(\boldsymbol{\eta}_*^{(m)}) \left( \delta^{(m)}(\boldsymbol{\eta}_*^{(m)}) - E[\tilde{\delta}(\boldsymbol{\eta}_*)] \right)^2 \quad (13)$$

The variance (13) must be understood as an indicator of the consensus among the models: small variances result from a strong agreement of individual model predictions while large variances reveal a divergence. Furthermore, as the weights are better informed, they get closer to 1 for the best models and to 0 for the worst models, and the variance decreases. This indicates that the uncertainty about model choice has been reduced.



In practice, we may wish to use XMA for predicting different QoI than the observed vector  $\bar{\delta}$ , either by direct extraction from the model or through post-processing of the solution. Examples of such QoI are given by flow properties at given locations in the flow, like velocity profiles, pressure or skin friction distributions. We denote  $\mathbf{\Delta} = (\Delta_1, \dots, \Delta_{N_\Delta})^T$  the vector of such unobserved QoI. Such outputs also depend on the flow scenario  $S$ , the equations of motion and the turbulence model, *i.e.*:

$$\Delta = M_\Delta(\mathbf{x}; S, \mathcal{F}_m, \boldsymbol{\theta}_{\mathcal{F}_m}) \quad (14)$$

where  $M_\Delta$  stands for a different postprocessed output of the same flow solver than  $M$ . The model aggregation (12) and variance equation (13) can be transposed to the quantity  $\Delta$ . Since no data is available to inform the weights for  $\Delta$ , we use the same weights as those learned for  $\tilde{\delta}$ :

$$\Delta(\boldsymbol{\eta}_*) = E[\tilde{\Delta}(\boldsymbol{\eta}_*)] = \sum_{m=1}^{N_M} w_m(\boldsymbol{\eta}_*^{(m)}) \Delta^{(m)}(\boldsymbol{\eta}_*^{(m)}) \quad (15)$$

and

$$Var[\tilde{\Delta}(\boldsymbol{\eta}_*)] = \sum_{m=1}^{N_M} w_m(\boldsymbol{\eta}_*^{(m)}) \left( \Delta^{(m)}(\boldsymbol{\eta}_*^{(m)}) - E[\Delta(\boldsymbol{\eta}_*)] \right)^2 \quad (16)$$

where  $\Delta^{(m)}$  is the  $\Delta$  output for the  $m$ -th model. Using the same weights for  $\delta$  and  $\Delta$  is reasonable as long as the deviations from observed to predicted quantities, of  $\tilde{\delta}$  are correlated to those of  $\Delta$ . The latter is a desirable property meaning that both  $\tilde{\delta}$  and  $\Delta$  are well predicted on the same locations. In this case, the space dependent weights in (15) and (16) will promote models where both  $\tilde{\delta}$  and  $\Delta$  are accurately predicted. As a result, we can also expect an efficient and accurate composite prediction (15).

## 2.2. Supervised regression

In order to enable XMA predictions at points  $\boldsymbol{\eta}_*$  outside the training set, a supervised regression method is used to reconstruct the weighting functions  $w_m(\boldsymbol{\eta}_*)$ . More precisely, we introduce supervised regressors for estimating the cost functions  $g_m$  at point  $\boldsymbol{\eta}_*$ , which are subsequently used to compute the weights.

In supervised regression, a set of input-output pairs (the training data set) is provided, the assigned goal being to learn the function that maps inputs to outputs [45]. Many well-known model class algorithms fall into this category: linear models [46], Support Vector Machines (SVM) and kernel methods [47], Gaussian Process Regression [48], Ensemble Methods based on trees [30] or Neural Networks [49], to cite just a few.

In the rest of the study, we use Random Forests (RF) [31], which are well-suited to large datasets and highly non-linear problems. In the present calculations we use the RF package available in the *scikit-learn python* module. The algorithm relies on four hyperparameters: (i) the number of trees, (ii) the maximum number of features evaluated during a splitting, (iii) the criterion considered for node splitting and (iv) the minimum number of samples in a leaf. The number of trees is fixed to a high value of 300, while the other three hyperparameters are optimized by grid

search. The grid search is performed from a  $K$ -fold splitting with  $K = 10$ .

We train  $N_M$  RF regressors modeling the relationship between the cost function  $g_m$  and the features  $\boldsymbol{\eta}^{(m)}$  for each of the component models. Input-output pairs of the form:  $\mathbf{C}_m = \{(\boldsymbol{\eta}_d^{(m)}, g_m(\boldsymbol{\delta}^m; \boldsymbol{\eta}_d^{(m)}, \bar{\boldsymbol{\delta}}_d, \sigma))\}_{d=1}^{N_\delta}$ ,  $m \in \{1, \dots, N_M\}$  are used for the training.

For predictions, either on scenarios on which we have reference data, or also on new scenarios, the features at the  $N_P$  cell nodes to be predicted are collected in a dataset  $\{\boldsymbol{\eta}_j^{(m)}\}_{j=1}^{N_P}$ . This dataset can be used as input to the RF regressors to make predictions on  $g_m$  and obtain the model weights.

As a result of the regression process, RF approximations  $\tilde{g}_m(\boldsymbol{\eta}^{(m)})$  of the cost function are eventually obtained for each component model, which are ultimately used to estimate the models' weights:

$$\tilde{w}_m(\boldsymbol{\eta}^{(m)}) = \frac{\tilde{g}_m(\boldsymbol{\eta}^{(m)})}{\sum_{j=1}^{N_M} \tilde{g}_j(\boldsymbol{\eta}^{(j)})}, \quad m \in \{1, \dots, N_M\} \quad (17)$$

In the following numerical experiments, we observed that  $g_m$  and  $\tilde{g}_m$  may sometimes take values approaching the machine zero for all  $m$ , making (17) becomes ill-conditioned, and possibly leading to incorrect results for the model weights. Since low values of the cost functions indicate overall low confidence in all of the component models, we introduce an empirical lower bound to the cost functions  $C$ : if the cost functions for all models are below  $C$  at a given point of the feature space, the XMA weights are simply returned to the uniform choice  $w_m = 1/N_M$ . We conducted a sensitivity analysis on the value of the cutoff-limit  $C$  and we observed no significant influence on the result for  $C \in [0.001, 0.15]$ . The value  $C = 0.001$  is thus retained for the rest of the study.

### 2.3. Input features

Switching from the space of geometrical coordinates to a space of input features is an effective method for generalizing model prediction to unseen geometries. In this work, we select a subset of 10 features among those initially proposed by Ling and Templeton [50]. The latter define a feature space whose elements are the vectors  $\boldsymbol{\eta} = (\eta_1, \dots, \eta_h, \dots, \eta_{10})^T$ . The list of input features used in this work is reported in Table 1, where  $U_i$  denotes the mean velocity component in the  $i$ th space direction,  $P$  the average pressure,  $\boldsymbol{\Omega}$  the mean rotation rate,  $\mathbf{S}$  the mean strain rate,  $k$  the turbulent kinetic energy,  $\varepsilon$  the turbulence dissipation rate,  $\rho$  the fluid density,  $\nu$  the kinematic viscosity,  $\nu_T$  the eddy viscosity, and  $\|\cdot\|$  is the Frobenius norm. Note that some turbulence models, e.g. the Spalart-Allmaras model considered later in this work, do not provide estimates of the turbulent kinetic energy  $k$ . In such cases, the feature is simply excluded from considerations.

## 3. Simulation setup and reference data

### 3.1. Test case description

In the following, the XMA algorithm is demonstrated for a flow problem of practical interest in turbomachinery, the turbulent flow through a compressor cascade. Specifically, we model the flow around the NACA 65 V103 – 220

Feature	Description	Formula	Feature	Description	Formula
$\eta_1$	Normalized $Q$ criterion	$\frac{\ \Omega\ ^2 - \ \mathbf{S}\ ^2}{\ \Omega\ ^2 + \ \mathbf{S}\ ^2}$	$\eta_6$	Viscosity ratio	$\frac{\nu_T}{100\nu + \nu_T}$
$\eta_2$	Turbulence intensity	$\frac{k}{0.5U_iU_i + k}$	$\eta_7$	Ratio of pressure normal stresses to normal shear stresses	$\frac{\sqrt{\frac{\partial P}{\partial x_i} \frac{\partial P}{\partial x_i}}}{\sqrt{\frac{\partial P}{\partial x_j} \frac{\partial P}{\partial x_j} + 0.5\rho \frac{\partial U_k^2}{\partial x_k}}}$
$\eta_3$	Turbulent Reynolds number	$\min\left(\frac{\sqrt{k}\lambda}{50\nu}, 2\right)$	$\eta_8$	Non-orthogonality marker between velocity and its gradient [51]	$\frac{\left U_k U_l \frac{\partial U_k}{\partial x_l}\right }{\sqrt{U_n U_n U_i \frac{\partial U_i}{\partial x_j} U_m \frac{\partial U_m}{\partial x_j} + \left U_i U_j \frac{\partial U_i}{\partial x_j}\right }}$
$\eta_4$	Pressure gradient along streamline	$\frac{U_k \frac{\partial P}{\partial x_k}}{\sqrt{\frac{\partial P}{\partial x_j} \frac{\partial P}{\partial x_j} U_i U_i + \left U_l \frac{\partial P}{\partial x_l}\right }}$	$\eta_9$	Ratio of convection to production of $k$	$\frac{U_i \frac{\partial k}{\partial x_i}}{\left u'_j u'_l S_{jl}\right  + U_l \frac{\partial k}{\partial x_l}}$
$\eta_5$	Ratio of turbulent time scale to mean strain time scale	$\frac{\ \mathbf{S}\ k}{\ \mathbf{S}\ k + \varepsilon}$	$\eta_{10}$	Ratio of total Reynolds stresses to normal Reynolds stresses	$\frac{\ \overline{u'_i u'_j}\ }{k + \ \overline{u'_i u'_j}\ }$

Table 1: List of input features used in this study.

Scenario	$S_1$	$S_2$	$S_3$	$S_4$
$\beta_1$	36.99°	39.97°	44.09°	49.2°
$Ma_1$	0.654	0.674	0.666	0.65
$Re_1$	302K	302K	298K	289K
Tu (%)	2.9	3.3	3.2	3.5

Table 2: Flow conditions for various compressor cascade scenarios.

linear compressor cascade, widely studied in the literature [52, 53, 54, 55, 56] and already used as a test case in our previous works [18, 19]. The cascade is representative of the mid-span section of a stator blade in a highly loaded axial compressor [52]. The blade aspect ratio being  $h/l = 1.36$ , it has been observed from the oil flow visualizations performed on the blade surface [57] that the flow "can be considered two-dimensional in the mid-span section" for the range of Mach and Reynolds numbers considered, which justifies the present choice of 2D RANS simulations. The cascade geometry and nomenclature (taken from Ref. [53]) are displayed in Fig. 1.

### 3.2. RANS solver and computational grid

The simulations are carried out with the CFD solver *elsA*, developed by ONERA [58]. The code solves the steady compressible RANS equations for Newtonian ideal gases by means of a cell-centered finite volume method on multi-block structured grids. The upwind scheme of Roe with second-order MUSCL extrapolation is used for approximating the inviscid fluxes, and a Gauss second-order scheme is used for the viscous fluxes. The solution is advanced to the steady state by using the first-order backward Euler scheme and local time stepping.

The computational domain contains a single blade profile, and periodic boundary conditions are applied at the upper and lower boundaries to simulate an infinite cascade. The domain extends from 0.5 axial chord upstream of

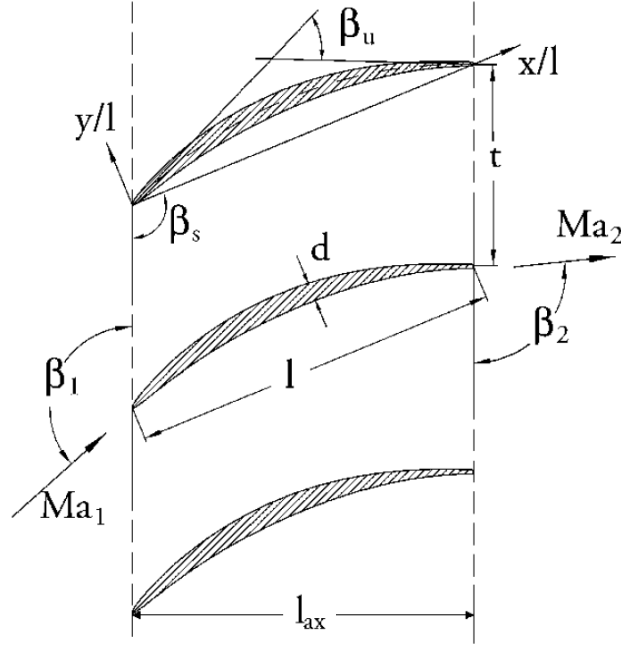


Figure 1: Sketch and design conditions of the NACA 65 V103 – 220 linear compressor cascade. Sketch copied on from [53].

the leading edge to 1.0 axial chord downstream the trailing edge. The top and bottom boundaries are separated by a distance equal to 0.59 axial chord, which also represents the gap between neighboring blades. No-slip adiabatic boundary conditions are applied at the blade wall, and characteristic conditions based on the Riemann invariants are imposed at the inlet and outlet boundaries. At the inlet, the total pressure, enthalpy and angle of attack are prescribed, whereas a constant static pressure is enforced at the outlet. The computational grid is composed by six matching blocs, for a total number of 30,880 cells. The near-wall grid resolution leads to an average height of the first cell closest to the wall (in wall coordinates) such that  $y^+ < 1.0$  on both the suction and the pressure side of the blade. We verified that, with such a resolution, the numerical solution had reached satisfactory mesh-independency. Convergence to the steady state is assumed when the  $L_2$  norm of the residuals has been reduced by six orders of magnitude with respect to the initial value.

### 3.3. Turbulence models

The XMA predictions reported in Section 4 are constructed from a multi-model ensemble of four concurrent linear-eddy-viscosity turbulence models (LEVM), selected amidst the most widely used in industrial practice. Baseline RANS simulations of the NACA 65 V103 – 220 cascade are conducted for each of the component LEVM and for all scenarios in  $\{S_1, S_2, S_3, S_4\}$ , i.e. a total of 16 baseline RANS. Such simulations constitute the components of the subsequent XMA procedure. An additional explicit algebraic Reynolds stress model (EARSM) is used to generate reference data for training and validation, as discussed in Section 3.4. The reader is referred to the original articles cited in the following for more details about the models in use.

### 3.3.1. Component turbulence models

**Spalart–Allmaras model [59]**: the most popular one-equation RANS model relies on a transport equation for an eddy-viscosity-like quantity  $\tilde{\nu}$ , which merges with turbulent viscosity  $\nu_t$  far from the walls.

**Wilcox  $k - \omega$  [4]**: the model relies on transport equations for the turbulent kinetic energy  $k$  and the specific dissipation rate  $\omega$ . The eddy viscosity is then obtained as  $\nu_t = k/\hat{\omega}$ , with  $\hat{\omega}$  a modified specific dissipation.

**Launder–Sharma  $k - \varepsilon$  [60]**: the model relies on transport equations for the turbulent kinetic energy  $k$  and the turbulent dissipation rate  $\varepsilon$ , the eddy viscosity being obtained as  $\nu_t = C_\mu k/\varepsilon$ , with  $C_\mu$  a constant, generally taken equal to 0.09.

**Smith  $k - L$  [61]**: the model was derived from the  $k - kL$  model of [62] with the aim of simplifying the wall functions in the  $kl$  equation. The model uses two transport equations for  $k$  and for the turbulence length scale  $L$ . The turbulent dissipation  $\varepsilon$  is connected to  $L$  through the following relation:  $\varepsilon = (2k)^{3/2}/B_1L$ .

### 3.3.2. Reference model

In addition to the component LEVM models used in the XMA, we also consider a reference model relying on a different constitutive relation for the Reynolds stress tensor, i.e. displaying a major structural difference in its mathematical formulation compared to LEVMs. EARSM are expected to provide a more accurate representation of turbulence anisotropy and rotation effects compared to LEVM. For that reason, the model is here introduced for the double purpose of generating training data for the XMA and assessing the model prediction. This allows generating any amount of training data for any QoI and for any flow scenario, enabling detailed parametric analyses and solution assessment (reported in Section 4) that could be hardly achieved with the limited high-fidelity datasets available in the literature. Precisely, we consider in the following the EARSM  $k - kL$  model of [63]. The latter models the anisotropy tensor through the Wallin-Johansson formulation [64], alongside Smith’s  $k - kL$  transport equation for computing the turbulent length and velocity scales [61].

### 3.4. Training data sets

High-fidelity data are collected for inferring the XMA mixture weighting functions in the feature space. More precisely we consider four cascade operating conditions or scenarios, described in Table 2. High-fidelity DNS and LES simulations exist in the literature for this cascade (e.g. [55, 56]), but unfortunately only limited results from those datasets are publicly accessible. This is why, for the aims of the present proof-of-concept study, we considered instead synthetic data sets generated through the reference EARSM  $k - kL$  model. The *elsA* RANS solver supplemented with the EARSM  $k - kL$  model is used to generate reference full fields for various flow quantities (including velocity, static and total pressure, and temperature) for each scenario in  $\{S_1, S_2, S_3, S_4\}$ . During preliminary tests (not reported for brevity), the reference flow-field quantities were used to investigate the effect of inferring the XMA model weights from various kinds of data. Numerical tests showed that the total pressure is the most informative quantity. Indeed,

that total pressure depends on both dynamic and thermodynamic quantities, and therefore it carries more information about the flow than pressure or velocity separately, and particularly about losses in the viscous boundary layers and wake. In the following, the total pressure is retained as the only observed quantity in the data set  $\bar{\delta}$ . Reference fields of the remaining flow quantities are used for validation only.

Two subsets of total pressure data are then extracted from the reference simulations, with the aim of investigating the effect of training set size on the learned XMA weights. Given the numerical solutions available at each point of the computational mesh for the four scenarios a first data set is constructed by collecting total pressure data at all mesh points, which we call the "big data" regime hereafter. The data are extracted at the mesh nodes, leading to a total of 40080 data. We also consider a "small data" training regime corresponding to selecting one over 8 mesh points in each mesh direction, leading to a total of 820 data points. Figure 2 displays the arrangement of numerical probes in the small data. The data are uniformly distributed across the grid, and no attempt was made to use optimal sensor placement (OSP) techniques or prior physical knowledge on the flow, since it was beyond the scope of the present work. Further research on optimal sensor placement is warranted in the future.

In the following, numerical experiments are conducted by training the XMA weighting functions against observations for a single flow scenario (i.e. by using total pressure data for the chosen scenario), or for several scenarios simultaneously (i.e. by using a concatenation of the total pressure datasets for the various scenarios). When multiple scenarios are used to build the training set, the same observation points are considered for all scenarios, but other choices are possible.

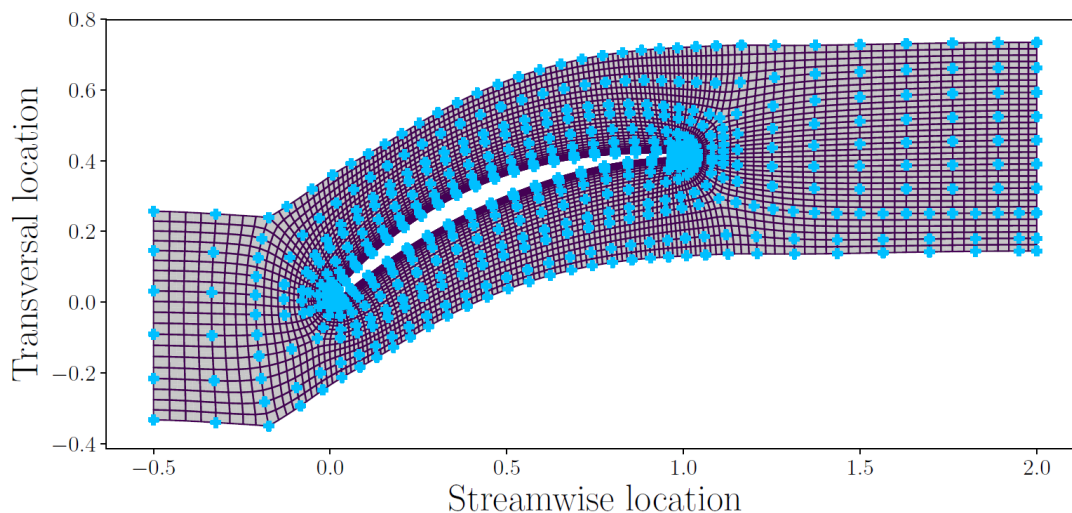


Figure 2: Locations of the observation points for the small data regime.  
For clarity, only one of four mesh vertices is represented.

#### 4. Results

In this section the XMA is applied to predict flow past the NACA 65 V103 cascade.

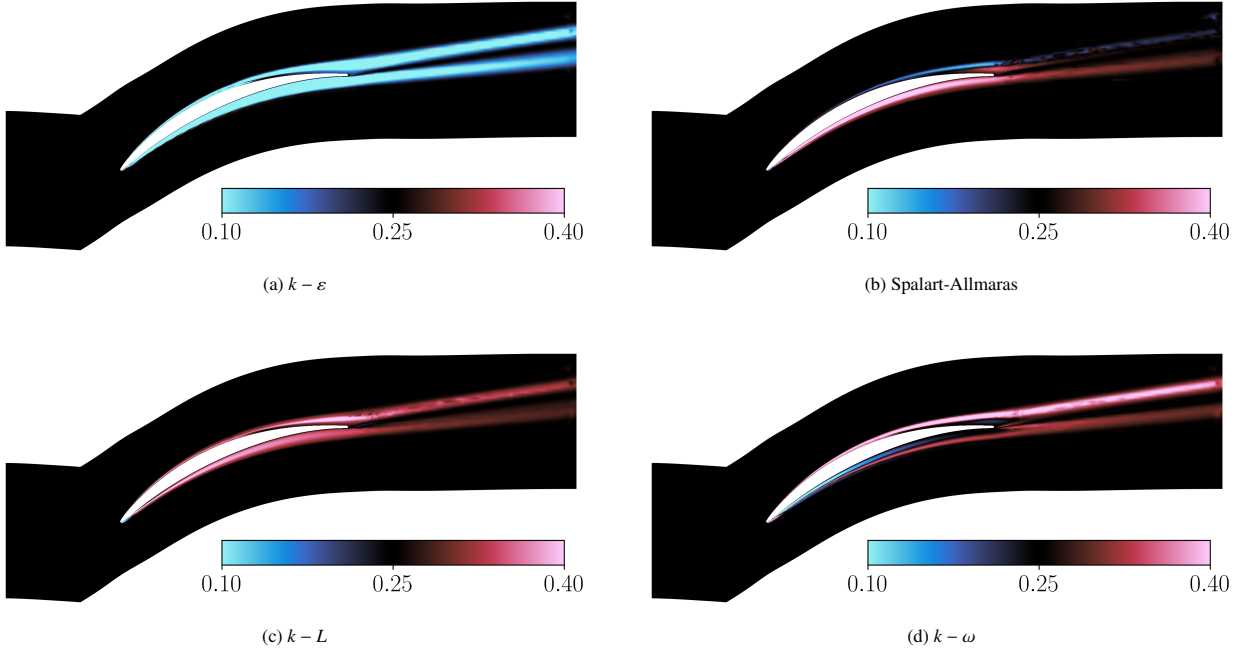


Figure 3: Iso-contours of the  $XMA_1$  weighting functions for the four component RANS models. Training and prediction on  $S_2$ .

As a first test, XMA is trained and tested on the same flow scenario (namely  $S_2$ ). A sensitivity study of the results to the hyperparameters of the XMA model is carried out. Afterwards, XMA is used for predicting a flow scenario not used for training. More precisely, we train XMA on three scenarios and we predict on the fourth. We choose to train the algorithm on scenarios  $\{S_2, S_3, S_4\}$  and predict on  $S_1$ , in order to have the angle of attack of the prediction scenario outside the range of the angles of attack of the training scenarios. As described in Section 3.1,  $S_1$  has a severely off-design angle of attack and also the lowest of the four available scenarios, which makes this scenario an extrapolation configuration and a challenging test case for assessing XMA predictions outside the training set.

#### 4.1. Training and prediction on scenario $S_2$

In this section, the XMA algorithm is trained on EARS  $k-kL$  reference total pressure data for scenario  $S_2$  and applied for the prediction of the full fields on the same scenario. To assess the effect of the number of training data two XMA models are constructed. The first one, noted  $XMA_1$  is trained on the complete data set (*i.e.* 40080 data) and corresponds to the big data regime; a second model, named  $XMA_2$  uses only 820 data, which corresponds to a scarce data regime. Of note, the second situation is the most likely to occur in practice, especially in the case of experimental measurements.

Fig. 3 presents the iso-contours of the weighting functions  $w_m$  for  $XMA_1$  and the four component RANS models. The predictions have been obtained in the feature space and then brought back in the geometrical space  $(x, y, z)$  to produce visualizations. We observe that all four models are assigned weights equal to  $1/4$  far from the blade, *i.e.* in the potential flow region. This is consistent with the theoretical expectation that RANS modeling does not affect

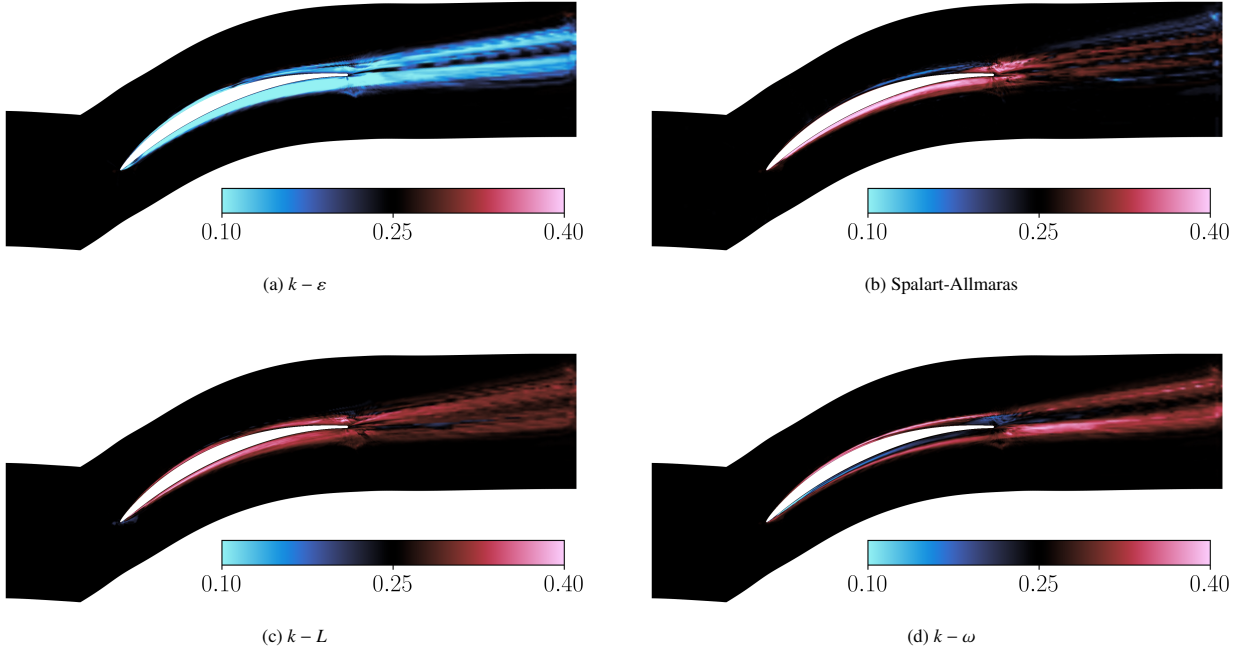


Figure 4: Iso-contours of the  $XMA_2$  weighting functions for the four component RANS models. Training and prediction  $S_2$ .

the potential region for the present flow with thin and attached boundary layers. As a consequence, the models are equally likely to capture the reference solution in that region. On the other hand, the models weights exhibit considerable differences in the vicinity of the blade and in the wake. Fig. 3a shows that the  $k - \epsilon$  model is generally associated with lower weights in the wake and on the suction and pressure sides, meaning that  $XMA_1$  has learned that  $k - \epsilon$  is the less likely to accurately predict the reference data in those regions, compared to the other models. The three remaining models are globally given higher weights. First, the Spalart-Allmaras model (see Fig. 3b) is assigned high weights at the pressure side and, to a minor extent, at the rear of the suction side, close to the trailing edge, while the weight tends to go down to  $1/4$  in the wake. Similarly, the  $k - L$  model (Fig. 3c) is given a very high weight at the suction side and a rather high weight at the pressure side. Finally, Fig. 3d presents the weighting function contours for the  $k - \omega$  model. This model is given the highest weight on the first half of the suction side, which is then continued by a thin and detached band of low weight on the second half of the suction side. A similar behavior is observed at the pressure side.

Fig. 4 presents the weighting function contours for  $XMA_2$ , trained with only 820 data. Similarly to Fig. 3a, the  $k - \epsilon$  model is given an overall lower weight than the other models. Overall, the contours are very similar to those obtained in the big data regime ( $XMA_1$ ), albeit a bit noisier. The observed noise is mostly caused by the interpolation errors. Nevertheless, the scarce data XMA results remain satisfactory and illustrate of potential of the proposed methodology for real-world applications with limited training data.

We now evaluate more quantitatively the quality of XMA training using different amounts of data by comparing the XMA prediction of the quantity used for training (total pressure) with the reference data. First, in Fig. 5 we report



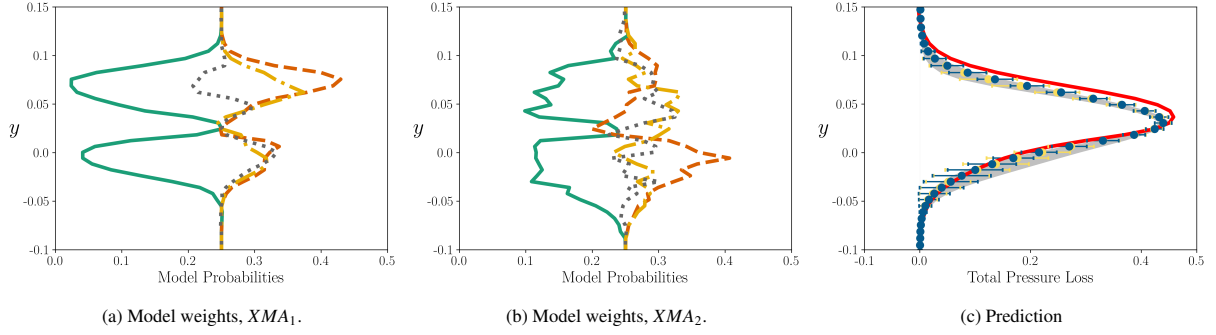


Figure 5: Profiles of the weighting functions and of the XMA prediction of the total pressure loss across the wake, at streamwise location  $\frac{x}{l} = 1.20$ . Solutions are reported for the big data ( $XMA_1$ ) and scarce data ( $XMA_2$ ) regimes. Training and prediction on  $S_2$  total pressure data.  $k - \varepsilon$  (—),  $k - \omega$  (---),  $k - L$  (- · - ·), Spalart-Allmaras (·····), reference data (—), accessible area  $\square$ ,  $E[\Delta] \pm 2\sqrt{\text{Var}[\Delta]}$  for  $XMA_1$  (●—),  $E[\Delta] \pm 2\sqrt{\text{Var}[\Delta]}$  for  $XMA_2$  (●—).

profiles of the the model weights and the corresponding XMA prediction for the normalized total pressure loss (defined as  $(Pt_{inlet} - Pt)/(Pt_{inlet} - P_{inlet})$  with  $Pt$  the total pressure,  $P$  the static pressure and *inlet* denoting the inflow boundary of the computational domain) at a given streamwise location across the wake ( $\frac{x}{l} = 1.20$ ). Solutions are reported for both the big data and the scarce data regimes. Inspection of the weight profiles across the wake (Figs 5a and 5b) shows that all weighting functions tend toward the uniform weighting of 1/4 in the potential region outside the wake. As observed previously in the weighting functions contour plots, the  $k - \varepsilon$  model is assigned a low weight throughout, whereas the other RANS models are given approximately equivalent higher values, with the Spalart-Allmaras model being assigned somewhat lower weight in the upper part of the wake, consistently with the lower weight it is assigned in the suction-side boundary layer. The scarce-data  $XMA_2$  exhibits a qualitatively similar behavior as  $XMA_1$ , with the different models being assigned weights of the same order of magnitude, but the weight profiles are noisier. This results from the RF regressor being less informed in this case. Despite that, both  $XMA_1$  and  $XMA_2$  provide smooth solutions, rather close to each other, as shown in Fig. 5c. In the figure, the two XMA predictions, with associated variances estimated from Eq. (13) are compared with the reference data. The grey-shaded region represents the convex hull of individual predictions from each component RANS model. Since XMA constructs a convex linear combination of the component models at each point, then the XMA solution must lie within that hull, which is called hereafter the accessible area. For the QoI at stake the accessible area encompasses the reference solution in the bottom part of the wake, unlike the outer part of it. The XMA solution captures well the reference in the bottom part despite a large discrepancy among the component models (illustrated by the wide accessible area) because it correctly assign high local weights to the best performing models, reducing the contribution of the worst performing one to the predictions. In the upper part of the wake, all models exhibit relative consensus on the wrong solution, a known limitation inherent to mixture models. In such a case, the variances (a measure of model consensus) are also small and do not encompass the reference either. However, XMA does a proper job of assigning higher weights to models providing the best possible agreement with the data. The scarce-data  $XMA_2$  tends to assign more similar weights to all component models, i.e. it discriminates less well well-performing from bad-performing models. Nevertheless,

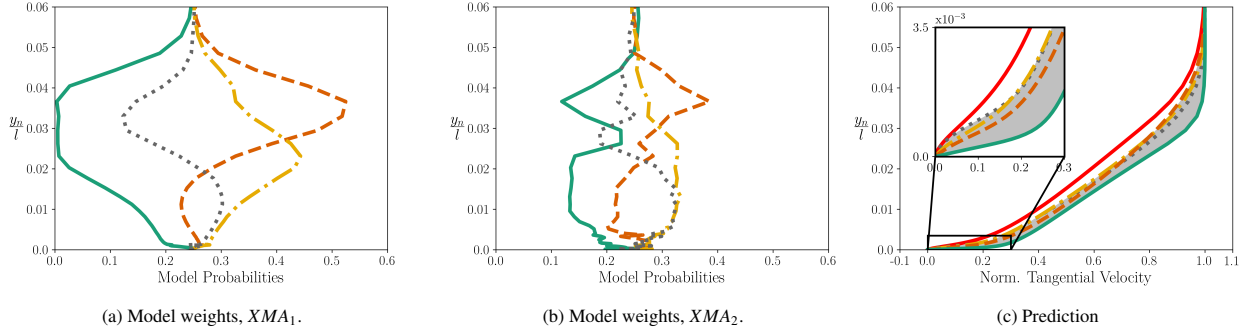


Figure 6: Profiles of the weighting functions (trained on  $S_2$ ) and of the tangential velocity for the four XMA component models, at streamwise location  $\frac{x}{l} = 0.9$  ( $S_2$ ). Solutions are reported for the big data ( $XMA_1$ ) and scarce data ( $XMA_2$ ) regimes.  $k - \epsilon$  (—),  $k - \omega$  (---),  $k - L$  (-·-·-), Spalart-Allmaras (·····), accessible area (■), reference data (—).

$XMA_2$  still provides improved performance overall, and much better performance than the worst model, showing that XMA prevents catastrophic loss of accuracy with respect to the common-practice choice of a single (possibly wrong) RANS model.

Next, XMA is used to reconstruct one-dimensional profiles of a flow quantity not used for training as a space-dependent linear combination of the baseline RANS profiles for the same quantity and the weighting functions. We focus more specifically on the prediction of tangential velocity profiles at chordwise location  $x/l = 0.9$ , *i.e.* at the rear of the suction side, *i.e.* in a region of adverse pressure gradient. Figure 6 shows the model weight distributions for  $XMA_1$  and  $XMA_2$  obtained after training on total pressure data. As observed previously, the weighting functions have similar trends (noisier for  $XMA_2$ ) but they exhibit sharper difference in the well-informed  $XMA_1$  than in  $XMA_2$ , which in turn tends to assign weights closer to the uniform distribution of  $1/4$ . Once again the  $k - \epsilon$  model is assigned much lower weights in both cases, while  $k - L$  and Spalart-Allmaras are preferred in the inner part of the boundary layer and  $k - \omega$  in the outer part. Figure 6c shows the accessible area, the reference data, and the individual component RANS solutions for the tangential velocity profiles (normalized with the velocity at boundary layer edge  $U_e$ ). The XMA algorithm is expected to rank the models in each region according to their agreement with the data, *i.e.* model weights should be a measure of the predictive accuracy of the corresponding component model. However, the weighting functions were learned from total pressure data, so we may wonder if they still provide a reasonable estimate of model accuracy for velocity profiles. We observe that  $k - \epsilon$ , the lowest weighted model, is the worst performing one in this case. The three other RANS models are closer to the reference, but the enlarged plot in the inset shows that the  $k - \omega$  model is less accurate than Spalart-Allmaras and  $k - L$  models close to the blade, and it is assigned a lower weight accordingly. Similarly, the Spalart-Allmaras is less accurate in the outer part of the boundary layer, and it is consistently assigned a very low weight in that region, both in  $XMA_1$  and  $XMA_2$ . This shows that, despite XMA is not directly trained on the predicted QoI, still it provides reasonable estimates of local model performance.

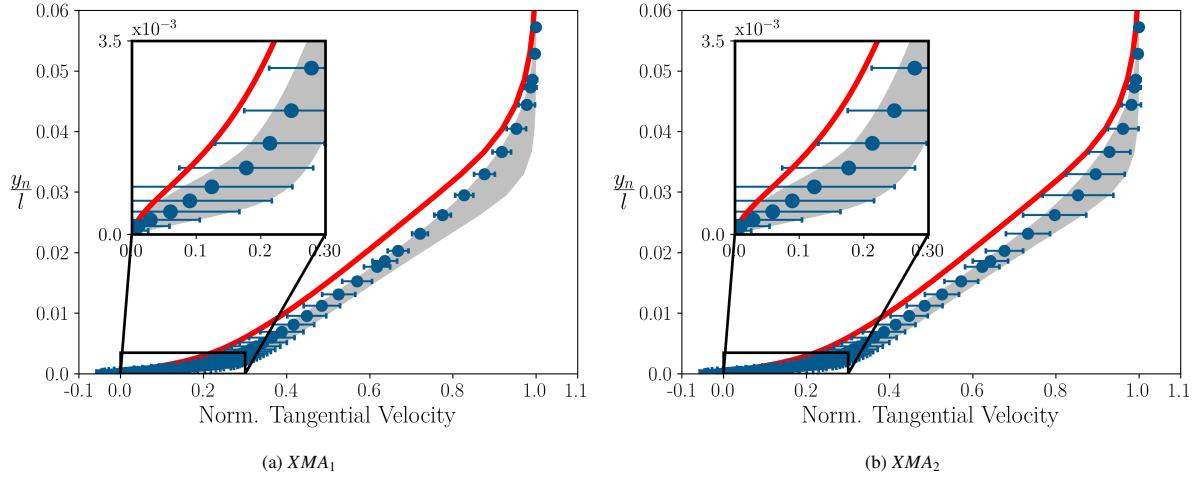


Figure 7: XMA prediction of the tangential velocity profile at  $\tilde{x} = 0.90$ ,  $S_2$ , for  $XMA_1$  and  $XMA_2$ . Reference data (—), accessible area  $\square$ ,  $E[\Delta] \pm 2\sqrt{\text{Var}[\Delta]}$  ( $\bullet$ —).

In Fig. 7 we present the reconstructed tangential velocity profiles at the same streamwise station, with error bars corresponding to twice the variance. The two panels correspond to  $XMA_1$  (Fig. 7a) and  $XMA_2$  (Fig. 7b), respectively. For both the big and the scarce data regimes, XMA predictions are in better agreement with the reference data than individual RANS models, showing that the algorithm is correctly preferring the best-performing model in each region of the boundary layer. Further, the variances provide an estimate of local model consensus, a measure of the risk of obtaining a significantly wrong solution if a single model was used to predict the flow. In the present case, the error bars encompass the reference data but, as already observed for the total pressure loss profiles, the area accessible by the component models does not. In other terms, the error bars must not be interpreted as the region where the true solution possibly lies, but simply as a measure of the uncertainty in the choice of a best-performing model. Of note, XMA assigns weights in such a way that the mixture prediction tends to the accessible area limit closer to the reference data. This effect is stronger for  $XMA_1$  than  $XMA_2$ , as previously observed for the total pressure loss, since bringing more information to the training set makes XMA more selective locally. This also results in larger variances for  $XMA_2$ , since all models are contributing rather significantly to the mixture everywhere, while in  $XMA_1$  only one or two best-performing models are assigned high weights in each region.

To provide an overview of the accuracy of XMA for various QoIs, in Fig. 8 we report the global mean squared errors (MSE) with respect to the reference data for four different QoI (pressure, velocity, skin friction and total pressure). The quantities are estimated at each point of the full computational mesh using XMA, and the predicted values are compared with the reference solution, except for the skin friction that is reconstructed only for mesh points along the blade wall. Of the four quantities, three were not used for model training. The errors of the four baselines RANS models are also reported for comparison. We observe that the baseline RANS models exhibit very different performance, even for a relatively simple 2-D configuration as the present compressor cascade. Additionally, model accuracy strongly depends on the QoI at stake. For instance, the Spalart-Allmaras model provides closer agreement

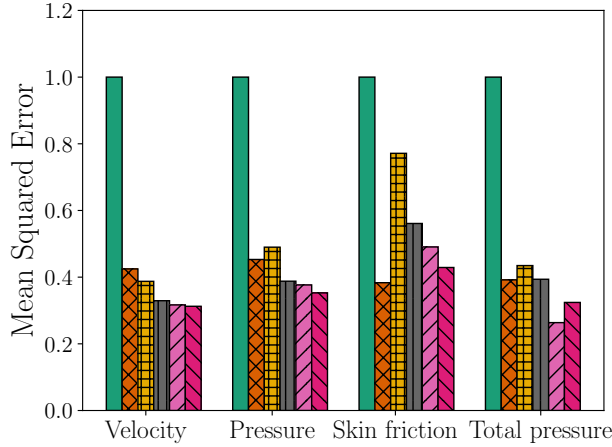


Figure 8: Mean-squared errors for four QoI (normalized by the MSE of the  $k-\epsilon$  model),  $S_2$ . XMA is trained on  $S_2$ .  $k-\epsilon$  model (■),  $k-\omega$  model (⊠),  $k-L$  model (▣) and Spalart-Allmaras model (■),  $XMA_1$  (▨),  $XMA_2$  (▩)

with the reference for velocity and pressure, while  $k-\omega$  provides a better estimate of the skin friction. The  $k-\epsilon$  is consistently less accurate than all other models for all QoI, which is in accordance with the fact that in Figs. 3a and 4a this model is systematically assigned a lower weight. The  $k-L$  model is the second least accurate model for the skin friction, in contradiction with Figs. 3c and 4c where the model is highly likely all over the blade. However, the weights have not been trained on skin friction data. Furthermore, the  $k-L$  model has been found to be particularly inaccurate close to leading edge, which radically deteriorates its average performance, although the prediction is reasonably good elsewhere. Turning now to XMA performance, we see from Fig. 8 that the XMA provides the most accurate predictions for three of the considered quantities and not only for the one used for training, even if the error for total pressure is lower than for the other quantities, as expected. For the skin friction, XMA performs worst than  $k-\omega$ , but is still more accurate than all the other component models. The results could be improved in the future by improving the selection and placement of training data. A particularly encouraging result is that both  $XMA_1$  and  $XMA_2$  are improving the results, despite the large difference in training set size, opening the way to the training of XMA from relatively scarce data sets (e.g. experimental datasets).

Finally, we complete the analysis of this case by presenting in Fig. 9 2-D contour plots of the expectancy and variance of the Mach number field, obtained with  $XMA_2$ . Despite the scarce data used for training, the 2-D fields are remarkably smooth. We verified that the same consideration holds for other QoI. As expected, high variances are observed in the near-wall region and in the turbulent wake, but also in regions of the external flow more strongly coupled with the viscous layers, typically, the regions with stronger pressure gradient directly affected by the boundary layer development.

#### 4.2. Prediction of an unseen scenario

In this Section we evaluate the ability of XMA at predicting an unseen flow scenario. More precisely, the XMA algorithm is trained simultaneously with data extracted from scenarios  $\{S_2, S_3, S_4\}$  and used to predict  $S_1$ . The training

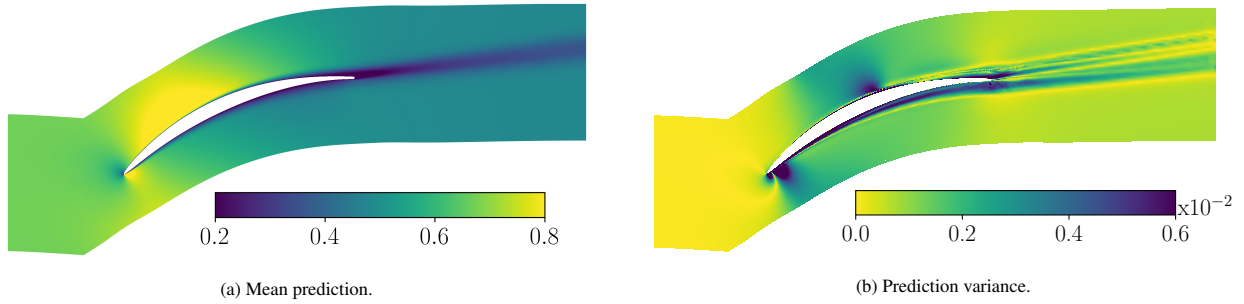


Figure 9: Iso-contours of the Mach number field predicted with  $XMA_2$  (training and prediction on  $S_2$ ).

data sets are constructed by concatenating total pressure data for the three scenarios. We note again  $XMA_1$  the big data regime, with a training set corresponding to full total pressure data for each flow scenario (*i.e.* 120240 data in total) and  $XMA_2$  the scarce data regime, with a training set constituted of 820 data for each scenario (*i.e.* 2460 data in total). Fig. 10 presents contour plots of the four model weighting functions  $w_m$  in the case of the  $XMA_1$ . The maps obtained for  $XMA_2$  are very similar and are omitted for the sake of brevity. As in the preceding tests,  $k - \varepsilon$  model is assigned low weights in all regions of interest, *i.e.* in the vicinity of the blade and in the wake. The Spalart-Allmaras model in Fig. 10b is assigned high weights on both pressure and suction side, as well as in the wake. The region close to the trailing edge is particularly associated with high weights, by contrast with the other models that are systematically assigned lower weights. In contrast with the prediction on  $S_2$ , Fig. 10c shows that the  $k - L$  model is assigned high weight only in the outer parts of the suction and pressure side boundary layers, but an intermediate weight of  $1/4$  on the pressure side and even low weight on the suction side close to the trailing edge. Finally,  $k - \omega$  model is assigned higher weights at the suction side, in the outer part of the boundary layer, and lower weights close to the wall inner part. At the pressure side on the contrary, the  $k - \omega$  model seems to be better performing in the inner part of the boundary layer rather than in the outer part.

Fig. 11 presents weighting functions and total pressure loss profiles at  $\frac{x}{l} = 1.20$  in the wake. Weighting function profiles for  $XMA_1$  and  $XMA_2$ , depicted in panels 11a and 11b, respectively, are rather similar, indicating that  $XMA_2$  is well informed in this case where we use three times more data than in the preceding example. As observed previously, using more data leads to sharper model weights. Due to the strong similarity of the weight distributions, the total pressure loss profiles predicted by  $XMA_1$  and  $XMA_2$  (panel 11c) are very close to each other. In both cases the reference data are captured almost perfectly, despite  $S_1$  has not been included in the training data set. The reason for that is that the reference solution is encompassed by the accessible area, so that XMA can potentially fit the data if the weight distributions are accurate. This appears to be the case in the present example, thus we conclude that XMA generalizes well to an extrapolation scenario.

In stark contrast with Fig. 5c, Fig. 11c presents a large variance on the prediction. This behavior can be sourced in two main reasons. The first reason is that the component RANS models predict very different solutions for this configuration, as indicated by the wide accessible area. The second reason is that the model weights are less sharp

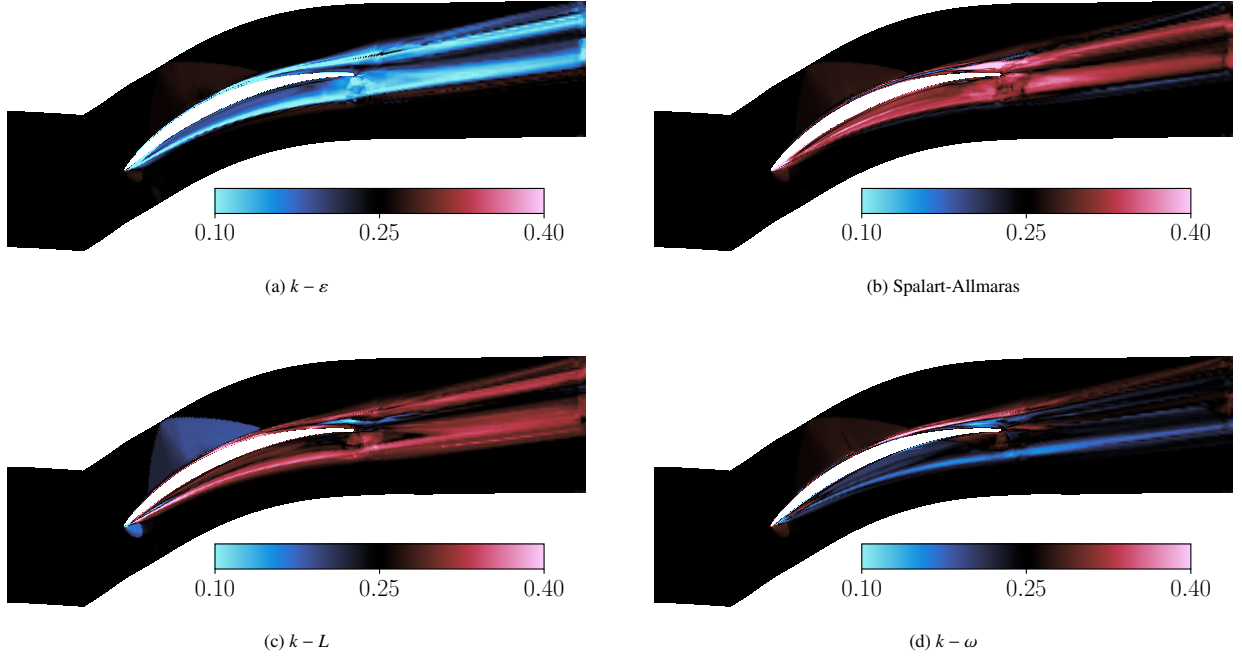


Figure 10: Isocontours of  $XMA_1$  weighting functions for the four component RANS models. Training on  $\{S_2, S_3, S_4\}$  and prediction on  $S_1$ .

on this extrapolation scenario than for an interpolation scenario, *i.e.* the models are weighted more uniformly. Both features warn the user about the fact that i) large model-form uncertainty exists and ii) XMA has to be trusted less than in the preceding example. That being said, the XMA is shown to be very effective at predicting QoI for which reference data lie within the accessible area. For that purpose, using a set of component models predicting quite diverse solutions is beneficial, because it widens the accessible area and increases the probability of pickling the local best-performing models if the weights are correctly modeled.

Fig. 12 model reports the weight profiles and XMA predictions of the tangential velocity profile at  $\frac{x}{l} = 0.90$ . For this quantity not used for training, the solution is less satisfactory, but still in rather good agreement with the reference

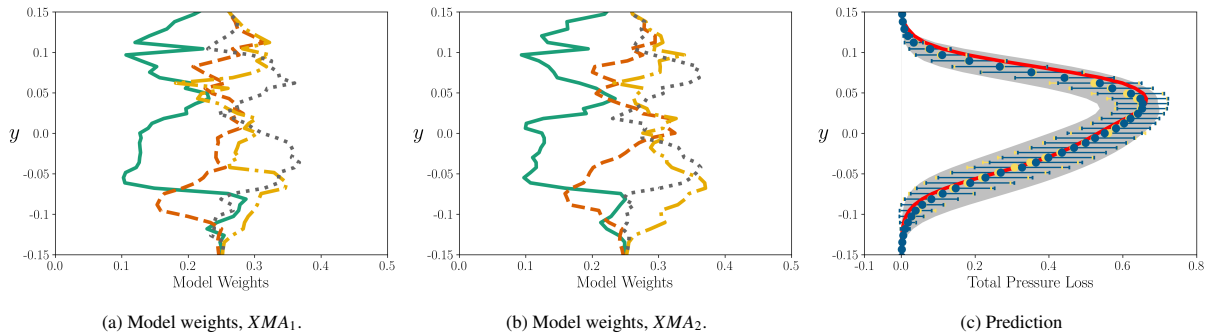


Figure 11: Profiles of the weighting functions (trained on  $\{S_2, S_3, S_4\}$  total pressure data) and of the total pressure loss across the wake at streamwise location  $\frac{x}{l} = 1.20$ . Solutions are reported for the big data ( $XMA_1$ ) and the scarce data ( $XMA_2$ ) regimes. Prediction on  $S_1$ .  $k - \varepsilon$  (—),  $k - \omega$  model (- - -),  $k - L$  (- · - ·), Spalart-Allmaras (·····), reference data (—), accessible area  $\square$ ,  $E[\Delta] \pm 2\sqrt{Var[\Delta]}$  for  $XMA_1$  (—●—),  $E[\Delta] \pm \sqrt{Var[\Delta]}$  for  $XMA_2$  (—●—).

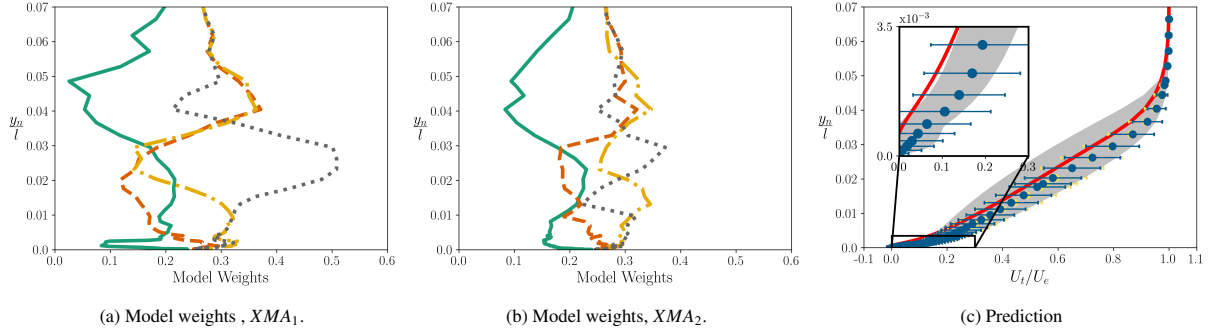


Figure 12: Profiles of the weighting functions (trained on  $\{S_2, S_3, S_4\}$  total pressure data) and of the tangential velocity profile at streamwise location  $\frac{x}{l} = 0.90$ . Solutions are reported for the big data ( $XMA_1$ ) and the scarce data ( $XMA_2$ ) regimes. Prediction on  $S_1$ .  $k - \varepsilon$  (—),  $k - \omega$  (---),  $k - L$  (-.-.-), Spalart-Allmaras (.....), reference data (—), accessible area  $\square$ ,  $E[\Delta] \pm 2\sqrt{\text{Var}[\Delta]}$  (—●—).

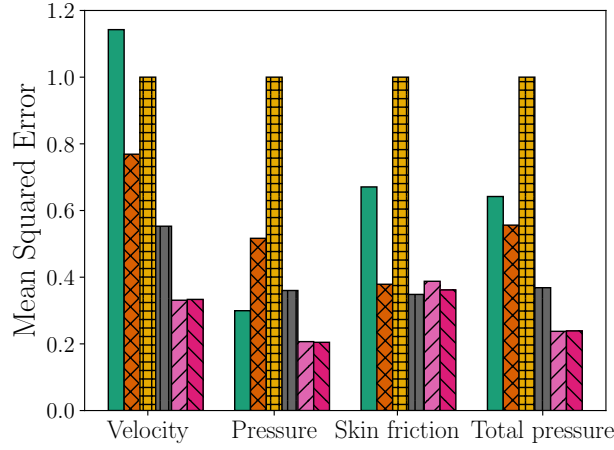


Figure 13: Mean-squared errors for four QoI (normalized by the MSE of the  $k - L$  model),  $S_1$ . XMA is trained on  $\{S_2, S_3, S_4\}$ .  $k - \varepsilon$  model (■),  $k - \omega$  model (■),  $k - L$  model (■) and Spalart-Allmaras model (■),  $XMA_1$  (■),  $XMA_2$  (■).

data. The predicted variances are rather large, providing a measure of RANS modelling uncertainties in the prediction.

Finally, in Fig. 13 we report the MSE for various QoI. In this case the results are normalized with the error of the  $k - L$  model, which exhibits the largest error on 3 out of 4 QoI.

The XMA predictions clearly improve the accuracy over the component RANS models, regardless of the QoI presented. For example, the MSE for the velocity is reduced by approximately 1/3 with respect to the best-performing baseline RANS model. Here again,  $XMA_1$  and  $XMA_2$  lead to similar MSE on average, showing that the scarce data regime is already sufficient to properly inform the mixture.

## 5. Conclusions

A novel space-dependent Model Aggregation (XMA) algorithm is introduced and assessed for improving Reynolds-Averaged predictions of turbulent flows while providing estimates of turbulence modeling uncertainties. XMA is a

multi-model ensemble technique that builds a convex linear combination of RANS solutions obtained by using a set of competing turbulence models, whose weight depend on a vector of well-chosen local flow features. A supervised machine learning algorithm (Random Forests) is used to regress the mixture weights as functions of the features from a training set of observed flow quantities. The weighting functions are based on a cost function that can be interpreted as the likelihood for a given model to capture the observed data, given the features. They can be interpreted as a relative score of performance assigned to each component model in the set of candidates. A convex linear combination of the individual RANS model solutions and the weighting functions is used to estimate an average RANS solution and its variance. The latter provides a measure of the uncertainty in the prediction, due to the lack of knowledge about the best-performing turbulence model for a given flow scenario and local flow features. In the numerical examples, we focus on a set of four linear eddy viscosity models (LEVM), widely used in engineering applications. Specifically, the Spalart-Allmaras, Launder-Sharma  $k - \varepsilon$ , Wilcox (2006)  $k - \omega$ , and Smith  $k - L$  models are used to build the XMA mixture. The approach is assessed for flow configurations of practical interest, namely, compressible turbulent flows through the NACA 65 V103 planar compressor cascade. For proving the interest of the proposed methodology, synthetic data are generated from RANS simulations based on an explicit algebraic Reynolds stress model (EARSIM), i.e. a model with a significantly different turbulence anisotropy structure compared to the LEVM. The EARSIM reference simulations, obtained for a set of four different operating conditions of the cascade (called "scenarios"), provides target values for all possible flow quantities for both training and validation. The synthetic data are used to investigate the influence of observed flow quantities and of the size of the training set on the quality of XMA predictions. For the configuration at stake, the total pressure, which depends on both kinematic and thermodynamic quantities, is used to train the XMA weights. Various training datasets are constructed by uniformly sampling the reference EARSIM solutions. The latter may contain observations extracted from a single flow scenario or by multiple scenarios simultaneously and both "big data" and "small data" regimes are considered. The first one corresponds to including total pressure data at all points of the computational mesh for the reference solution(s). The second one corresponds to extracting information at one mesh point over 8, leading to a dataset of only 820 data if a single scenario is included.

When XMA is trained on a single scenario and used to predict the same scenario, the predicted fields of the observed quantity do not match the reference data perfectly, due to the structural deficiencies of the underlying LEVM, whose individual solutions do not encompass the reference once everywhere in the flow. However, on the average, XMA consistently improves the results over any of the component models, because it consistently assigns higher weighting to the best performing models in each flow region. Interestingly, XMA does not only improve the prediction for the flow quantity used for training, but also for unobserved quantities that are reasonably well correlated with the preceding one, such as the velocity field. Additionally, the learned weighting functions and component solutions can be used to estimate the variance of the XMA estimate, which represents a measure of the consensus among the candidate models about what the solution should be. Relatively similar results are obtained for both for the big and scarce training sets, with the accuracy increasing and the variance decreasing with the size of the training set.

Afterward, XMA is trained against three flow scenarios and used to predict a fourth one, whose operating condi-



tions are not within the range of operating conditions of the calibration scenarios. For such extrapolation situation, the XMA shows very good generalization abilities, providing a solution that is overall more accurate than any of the component models for most flow quantities of interest. In this case however, the variances are larger, warning the user about the trustfulness of the results.

The present XMA relies on "on the shelf" component turbulence models, not specifically calibrated for the configuration of interest. Additionally, no attempt was done to optimize the placement of observation points used for model training. Thus, possible future improvements consist in simultaneously calibrating the models and training the weighting functions, as well as utilizing optimal sensor placement techniques (e.g. [65]) for selecting the training data. Further work on the choice of the flow features used to describe the model weights is also planned.

## 6. Acknowledgement

The present work was co-funded by Safran Tech and ANRT (Agence Nationale de la Recherche Technologique) under CIFRE Grant N. N2018/1370. The authors also thank CMasher for providing the colormaps used in the present plots.

## References

- [1] T. Oden, R. Moser, and O. Ghattas. Computer predictions with quantified uncertainty, part i. *SIAM News*, 43(9), 2010.
- [2] S.B. Pope. *Turbulent flows*. Cambridge university press, 2000.
- [3] H. Choi and P. Moin. Grid-point requirements for large eddy simulation: Chapman’s estimates revisited. *Physics of Fluids*, 24:015105, 2012.
- [4] D. C. Wilcox. *Turbulence modeling for CFD*. DCW Industries , La Canada, CA, 2006.
- [5] P. Spalart. Philosophies and fallacies in turbulence modeling. *Progress in Aerospace Science*, 74:1–15, 2015.
- [6] H. Xiao and P. Cinnella. Quantification of model uncertainty in RANS simulations: A review. *Progress in Aerospace Sciences*, 108:1–31, 2019.
- [7] S. Cheung, T. A. Oliver, E. E. Prudencio, S. Prudhomme, and R. D. Moser. Bayesian uncertainty analysis with applications to turbulence modeling. *Reliability Engineering & System Safety - RELIAB ENG SYST SAFETY*, 96:1137–1149, 09 2011.
- [8] T. A. Oliver and R. D. Moser. Bayesian uncertainty quantification applied to RANS turbulence models. In *Journal of Physics: Conference Series*, volume 318, page 042032. IOP Publishing, 2011.
- [9] Modeling of structural uncertainties in Reynolds-averaged Navier-Stokes closures.
- [10] W. N. Edeling, P. Cinnella, and R. Dwight. Predictive RANS simulations via Bayesian model-scenario averaging. *Journal of Computational Physics*, 275:65–91, 2014.
- [11] C. Górlé and G. Iaccarino. A framework for epistemic uncertainty quantification of turbulent scalar flux models for Reynolds-Averaged Navier-Stokes simulations. *Physics of Fluids*, 25(5):055105, 2013.
- [12] R. L. Thompson, A. Mishra, G. Iaccarino, W. Edeling, and L. Sampaio. Eigenvector perturbation methodology for uncertainty quantification of turbulence models. *Physical Review Fluids*, 4(4):044603, 2019.
- [13] P. D. A. Platteeuw, G. J. A. Loeven, and H. Bijl. Uncertainty quantification applied to the  $k$ - $\epsilon$  model of turbulence using the probabilistic collocation method. In *10th AIAA Non-Deterministic Approaches Conference*, 2008. Paper no.: 2008-2150.
- [14] W. N. Edeling, P. Cinnella, R. P. Dwight, and H. Bijl. Bayesian estimates of parameter variability in the  $k$ - $\epsilon$  turbulence model. *Journal of Computational Physics*, 258:73–94, 2014.
- [15] L. Margheri, M. Meldi, M. V. Salvetti, and P. Sagaut. Epistemic uncertainties in RANS model free coefficients. *Computers & Fluids*, 102:315–335, 2014.
- [16] S. V. Poroseva, M. Y. Hussaini, and S. L. Woodruff. Improving the predictive capability of turbulence models using evidence theory. *AIAA Journal*, 44(6):1220–1228, 2006.
- [17] W. N. Edeling, M. Schmelzer, R. Dwight, and P. Cinnella. Bayesian predictions of Reynolds-averaged Navier–Stokes uncertainties using maximum a posteriori estimates. *AIAA Journal*, 56(5):2018–2029, 2018.
- [18] M. de Zordo-Banliat, X. Merle, G. Dergham, and P. Cinnella. Bayesian model-scenario averaged predictions of compressor cascade flows under uncertain turbulence models. *Computers & Fluids*, 201:104473, 2020.
- [19] M. de Zordo-Banliat, X. Merle, G. Dergham, and P. Cinnella. Estimates of turbulence modeling uncertainties in naca65 cascade flow predictions by bayesian model-scenario averaging. *International Journal of Numerical Methods for Heat & Fluid Flow*, 32:1398–1414, 2022.
- [20] D. Draper. Assessment and propagation of model uncertainty. *Journal of the Royal Statistical Society: Series B (Methodological)*, 57(1):45–70, 1995.

- [21] J. A. Hoeting, D. Madigan, A. E. Raftery, and C. T. Volinsky. Bayesian model averaging: a tutorial. *Statistical science*, 14(4):382–401, 1999.
- [22] G. Stoltz. Agrégation séquentielle de prédicteurs : méthodologie générale et applications à la prévision de la qualité de l’air et à celle de la consommation électrique. *Journal de la Société Française de Statistique*, 151(2):41, 2010.
- [23] R. Deswarte, V. Gervais, G. Stoltz, and S. Da Veiga. Sequential model aggregation for production forecasting. *Computational Geosciences*, 23(5):1107–1124, 2019. Publisher: Springer Verlag.
- [24] M. Devaine, P. Gaillard, Y. Goude, and G. Stoltz. Forecasting electricity consumption by aggregating specialized experts: A review of the sequential aggregation of specialized experts, with an application to Slovakian and French country-wide one-day-ahead (half-)hourly predictions. *Machine Learning*, 90(2):231–260, 2013.
- [25] A. Blum. Empirical Support for Winnow and Weighted-Majority Algorithms: Results on a Calendar Scheduling Domain. *Machine Learning*, 26(1):5–23, 1997.
- [26] N. Littlestone. Learning Quickly When Irrelevant Attributes Abound: A New Linear-Threshold Algorithm. *Machine Learning*, 2(4):285–318, 1988.
- [27] A. DeSantis, G. Markowsky, and M. N. Wegman. Learning probabilistic prediction functions. In *[Proceedings 1988] 29th Annual Symposium on Foundations of Computer Science*, pages 110–119, October 1988.
- [28] N. Cesa-Bianchi, Y. Freund, D. P. Helmbold, D. Haussler, R. E. Schapire, and M. K. Warmuth. How to use expert advice. In *Proceedings of the twenty-fifth annual ACM symposium on Theory of Computing*, STOC ’93, pages 382–391, New York, NY, USA, June 1993. Association for Computing Machinery.
- [29] N. Littlestone and M. K. Warmuth. The Weighted Majority Algorithm. *Information and Computation*, 108(2):212–261, February 1994.
- [30] L. Breiman. Bagging predictors. *Machine learning*, 24:123–140, 1996.
- [31] L. Breiman. Random forests. *Machine learning*, 45:5–32, 2001.
- [32] R. E. Schapire, Y. Freund, P. Bartlett, and W. S. Lee. Boosting the margin: a new explanation for the effectiveness of voting methods. *The annals of statistics*, 26, 1998.
- [33] R. A. Jacobs, M. I. Jordan, S. J. Nowlan, and G. E. Hinton. Adaptive Mixtures of Local Experts. *Neural Computation*, 3:79–87, 1991.
- [34] S. E. Yuksel, J. N. Wilson, and P. D. Gader. Twenty Years of Mixture of Experts. *IEEE transactions on neural networks and learning systems*, 23(8):1177–1193, 2012.
- [35] M. I. Jordan and R. A. Jacobs. Hierarchical mixtures of experts and the EM algorithm. *Neural Computation*, 6(2):181–214, 1994.
- [36] J. S. Bridle. Probabilistic Interpretation of Feedforward Classification Network Outputs, with Relationships to Statistical Pattern Recognition. In *Neurocomputing*, NATO ASI Series, pages 227–236, Berlin, Heidelberg, 1990. Springer.
- [37] B. Gao and L. Pavel. On the Properties of the Softmax Function with Application in Game Theory and Reinforcement Learning, August 2018. arXiv:1704.00805 [cs, math].
- [38] A. P. Dempster, N. M. Laird, and D. B. Rubin. Maximum Likelihood from Incomplete Data via the EM Algorithm. *Journal of the Royal Statistical Society. Series B (Methodological)*, 39(1):1–38, 1977. Publisher: [Royal Statistical Society, Wiley].
- [39] T. Baldacchino, E. J. Cross, K. Worden, and J. Rowson. Variational Bayesian mixture of experts models and sensitivity analysis for nonlinear dynamical systems. *Mechanical Systems and Signal Processing*, 66-67:178–200, 2016.
- [40] Q. Yu, S. N. MacEachern, and M. Peruggia. Clustered Bayesian model averaging. *Bayesian Analysis*, 8(4):883–908, 2013.
- [41] K. Rahman, S. Shang, M. Shahid, and Y. Wen. Hydrological evaluation of merged satellite precipitation datasets for streamflow simulation using SWAT: A case study of Potohar Plateau, Pakistan. *Journal of Hydrology*, 587:125040, 2020.
- [42] I. Abdallah, K. Tatsi, and E. Chatzi. Unsupervised local cluster-weighted bootstrap aggregating the output from multiple stochastic simulators. *Reliability Engineering & System Safety*, 199:106876, 2020.
- [43] W. N. Edeling, P. Cinnella, R. Dwight, and H. Bijl. Bayesian estimates of parameter variability in the  $k$ - $\epsilon$  turbulence model. *Journal of Computational Physics*, 258:73–94, 2014.
- [44] E.J. Parish and K. Duraisamy. A paradigm for data-driven predictive modeling using field inversion and machine learning. *Journal of Computational Physics*, 305:758–774, 2016.
- [45] S. Russell and P. Norvig. *Artificial Intelligence: a Modern Approach, fourth edition*. 2020.
- [46] C. M. Bishop. *Pattern Recognition and Machine Learning*. Springer, 2006.
- [47] C. Cortes and V. Vapnik. Support-vector networks. *Machine learning*, 1995.
- [48] C. K. Williams and C. E. Rasmussen. *Gaussian processes for machine learning*. MIT press Cambridge, MA, 2006.
- [49] G. E. Hinton, S. Osindero, and Y. Teh. A Fast Learning Algorithm for Deep Belief Nets. *Neural Computation*, 18(7):1527–1554, 2006.
- [50] J. Ling and J. Templeton. Evaluation of machine learning algorithms for prediction of regions of high Reynolds averaged Navier Stokes uncertainty. *Physics of Fluids*, 27(8):085103, 2015.
- [51] C. Gorle, M. Emory, and G. Iaccarino. RANS modeling of turbulent mixing for a jet in supersonic cross flow: model evaluation and uncertainty quantification. In *THMT-12. Proceedings of the Seventh International Symposium On Turbulence Heat and Mass Transfer*, 2012.
- [52] R. Leipold, M. Boese, and L. Fottner. The influence of technical surface roughness caused by precision forging on the flow around a highly loaded compressor cascade. *Journal of turbomachinery*, 122(3):416–424, 2000.
- [53] L. Hilgenfeld, P. Cardamone, and L. Fottner. Boundary layer investigations on a highly loaded transonic compressor cascade with shock/laminar boundary layer interactions. *Proceedings of the Institution of Mechanical Engineers, Part A: Journal of Power and Energy*, 217(4):349–356, 2003.
- [54] J. Iseler, L. Hilgenfeld, and M. Pfitzner. Investigations of the boundary layer on a highly loaded compressor cascade with wake-induced transition. In *Turbo Expo: Power for Land, Sea, and Air*, 2006.
- [55] T. A. Zaki, J. G. Wissink, W. Rodi, and P. A. Durbin. Direct numerical simulations of transition in a compressor cascade: the influence of free-stream turbulence. *Journal of Fluid Mechanics*, 665:57–98, 2010.
- [56] J. Leggett, S. Priebe, R. Sandberg, V. Michelassi, and A. Shabbir. Detailed investigation of RANS and LES predictions of loss generation in an axial compressor cascade at off design incidences. In *ASME Turbo Expo 2016: Turbomachinery Technical Conference and Exposition*. American Society of Mechanical Engineers Digital Collection, 2016.
- [57] R. M. Bell and L. Fottner. Investigations of shock/boundary-layer interaction in a highly loaded compressor cascade. In *Turbo Expo: Power*

- for *Land, Sea, and Air*, volume 78781, page V001T01A016. American Society of Mechanical Engineers, 1995.
- [58] L. Cambier, S. Heib, and S. Plot. The ONERA elsA CFD software: input from research and feedback from industry. *Mechanics & Industry*, 14(3):159–174, 2013.
  - [59] P. R. Spalart and S. R. Allmaras. One-equation turbulence model for aerodynamic flows. *Recherche aerospaciale*, (1):5–21, 1994.
  - [60] B. E. Launder and B. I. Sharma. Application of the energy-dissipation model of turbulence to the calculation of flow near a spinning disc. *Letters in heat and mass transfer*, 1(2):131–137, 1974.
  - [61] B. R. Smith. A near wall model for the k-L two equation turbulence model. In *Fluid Dynamics Conference*, page 2386, 1994.
  - [62] B. R. Smith. The k-kL turbulence model and wall layer model for compressible flows. In *AIAA Paper 90-1483*, 1990.
  - [63] H. Bézard and T. Daris. Calibrating the length scale equation with an explicit algebraic Reynolds stress constitutive relation. In *Engineering turbulence modelling and experiments 6*, pages 77–86. Elsevier, 2005.
  - [64] S. Wallin and A. V. Johansson. An explicit algebraic Reynolds stress model for incompressible and compressible turbulent flows. *Journal of Fluid Mechanics*, 403:89–132, 2000.
  - [65] V. Mons, J.C. Chassaing, and P. Sagaut. Optimal sensor placement for variational data assimilation of unsteady flows past a rotationally oscillating cylinder. *Journal of Fluid Mechanics*, 823:230–277, 2017.